High-harmonic spectroscopy of coherent lattice dynamics in graphene

Navdeep Rana,[1] M. S. Mrudul,[1] Daniil Kartashov,[2] Misha Ivanov,[3] and Gopal Dixit[1,*]
[1]*Department of Physics, Indian Institute of Technology Bombay, Powai, Mumbai 400076, India*
[2]*Institute of Optics and Quantum Electronics, Friedrich-Schiller University Jena, Max-Wien-Platz 1, 07743 Jena, Germany*
[3]*Max-Born Straße 2A, D-12489 Berlin, Germany*

(Received 1 March 2022; revised 5 July 2022; accepted 2 August 2022; published 18 August 2022)

High-harmonic spectroscopy of solids is a powerful tool, which provides access to both electronic structure and ultrafast electronic response of solids, from their band structure and density of states to phase transitions, including the emergence of the topological edge states, to the PetaHertz electronic response. However, in spite of these successes, high-harmonic spectroscopy has hardly been applied to analyze the role of coherent femtosecond lattice vibrations in the attosecond electronic response. Here we study coherent phonon excitations in monolayer graphene to show how high-harmonic spectroscopy can be used to detect the influence of coherent lattice dynamics, particularly longitudinal and transverse optical phonon modes, on the electronic response. Coherent excitation of the in-plane phonon modes results in the appearance of sidebands in the spectrum of the emitted harmonic radiation. We show that the spectral positions and the polarization of the sideband emission offer a sensitive probe of the dynamical symmetries associated with the excited phonon modes. Our work brings the key advantage of high-harmonic spectroscopy—the combination of subfemtosecond to tens of femtoseconds temporal resolution—to the problem of probing phonon-driven electronic response and its dependence on the dynamical symmetries in solids.

DOI: 10.1103/PhysRevB.106.064303

I. INTRODUCTION

Strong-field driven high-harmonic generation (HHG) is a nonlinear frequency up-conversion process, which emits radiation at integer multiples of the incident laser frequency [1]. Taking advantage of major technical advances in midinfrared sources, the pioneering experiments [2] have extended HHG from gases to solids, stimulating intense research into probing electron dynamics in solids on the natural timescale. Today, high-harmonic spectroscopy has been employed to probe different static and dynamic properties of solids, such as band dispersion [3–6], density of states [7], band defects [8,9], valley pseudospin [10–12], Bloch oscillations [13], topology and light-driven phase transitions, including strongly correlated systems [14–23], and even combine attosecond temporal with picometer spatial resolution of electron trajectories in lattices [24].

Availability of midinfrared light sources also enables coherent excitation of a desired phonon mode by tuning the polarization and frequency of the laser pulse [25]. Yet, the analysis of the effect of coherent lattice dynamics on high-harmonic generation in solids appears lacking, apart from a lone experiment [26]. This situation stands in stark contrast to molecular gases, where high-harmonic spectroscopy has been extensively employed to probe nuclear motion in various molecules [27–32]. Present work aims to fill this gap and highlight some of the capabilities offered by high-harmonic spectroscopy in time resolving the interplay of femtosecond lattice and attosecond electronic motions. Such interplay is essential for many fundamental phenomena, including thermal conductivity [33], optical reflectivity [34,35], structural phase transition [36,37], heat capacity [38], and optical properties [39,40].

Various spectroscopic methods have been developed to excite and probe phonons, see, e.g., Refs. [41–52], but their temporal resolution is limited by the length of the pulses used. Large coherent bandwidth of high-harmonic signals offers sub-laser-cycle temporal resolution and the possibility to time resolve the impact of lattice distortions on the faster electronic response.

One difficulty in tracking lattice vibrations via highly nonlinear optical response stems from their small amplitude. If the corresponding changes in both the band structure and couplings are similarly small, the high-harmonic response hardly changes. Yet, large distortions are not needed if the excited phonon mode dynamically changes the symmetry of the unit cell. Here we show how coherent phonon dynamics and the associated changes in the lattice symmetry are encoded in the electronic response and the harmonic signal, and how the subcycle temporal resolution inherent in the harmonic signal can be used to track the interplay of electronic and lattice dynamics.

We analyze monolayer graphene, which belongs to $\mathbf{D}_{6h}$ point group symmetry; see Fig. 1(a). It exhibits six phonon branches: three optical and three acoustic. Here we focus on the former. Out of the three optical phonon modes, one is out of plane and the two others are in-plane modes. We will consider only the in-plane modes. The lattice vibrations corresponding to the in-plane longitudinal optical (iLO) and

*gdixit@phy.iitb.ac.in

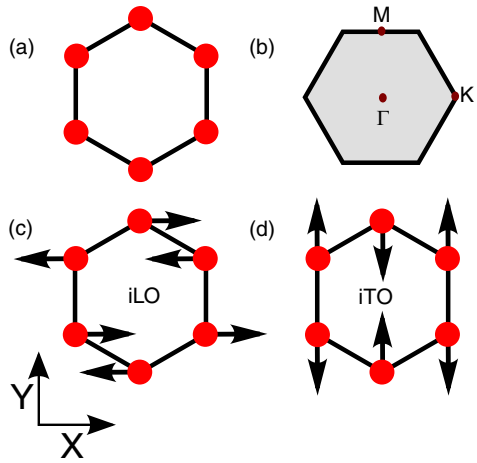

FIG. 1. Hexagonal honeycomb structure of graphene and associated in-plane phonon modes. (a) Real-space structure of graphene. (b) Brillouin zone in momentum space with Γ, M, and K as the high symmetry points. Panels (c) and (d) are the sketches of atomic vibrations associated with the degenerate E_{2g} phonon modes in real space. Here, modes are labeled as (c) in-plane longitudinal optical (iLO) phonon mode and (d) in-plane transverse optical (iTO) phonon mode, respectively.

the in-plane transverse optical (iTO) E_{2g} modes are shown in Figs. 1(c) and 1(d), respectively. The two modes are degenerate at the Γ point, with the phonon frequency equal to 194 meV (oscillation period ∼21 fs [53]); both are Raman active and can be excited with a resonant pulse pair or impulsively by a short pulse with bandwidth covering 194 meV. Moreover, it is possible to selectively excite either iLO or iTO coherent phonon mode by tuning the polarization of the pump pulse either along the Γ − K or Γ − M direction, respectively.

Coherent lattice dynamics should in general introduce periodic modulations of the system parameters and thus of its high-harmonic response. In the frequency domain, such modulations add sidebands to the main peaks in the harmonic spectrum. We shall see that their position and polarization encode the information about the frequency and the symmetry of the excited phonon mode, respectively.

II. THEORETICAL METHOD

Carbon atoms are arranged at the corners of a hexagon in the honeycomb lattice of the graphene. The unit cell of graphene has a two-atom basis, usually denoted as A and B atoms. The corresponding Brillouin zone in momentum space is shown in Fig. 1(b), where Γ, M, and K are the high-symmetry points. In our convention, the zigzag and armchair directions of graphene are along the X axis (Γ − K direction) and Y axis (Γ − M direction), respectively.

The electronic ground state of the graphene is described by the nearest-neighbor tight-binding approximation and the corresponding Hamiltonian is written as

$$\hat{\mathcal{H}}_{\mathbf{k}} = -\gamma_0 \sum_{i\in nn} e^{i\mathbf{k}\cdot\mathbf{d}_i} \hat{a}^\dagger_{\mathbf{k}} \hat{b}_{\mathbf{k}} + \text{H.c.} \tag{1}$$

Here, the summation is over the nearest-neighbor atoms. γ_0 is the nearest-neighbor hopping energy, which is chosen to be 2.7 eV. $\mathbf{d}_i$ is the separation vector between an atom with its nearest neighbor, such that $|\mathbf{d}_i| = a = 1.42$ Å is the interatomic distance, for a lattice parameter a_0 of 2.46 Å. $\hat{a}^\dagger_k(\hat{b}_k)$ is the creation (annihilation) operator for atom A (B) in the unit cell. The low-energy band structure of graphene is obtained by solving Eq. (1) and has zero band gap and exhibits linear dispersion at K points in the Brillouin zone.

We treat lattice dynamics classically and assume that atoms perform harmonic oscillations for short displacements from their equilibrium positions. The displacement vector for a particular phonon mode is expressed as

$$\mathbf{q}(t) = q_0\, \hat{\mathbf{e}}\, \text{Re}(e^{i\omega_{ph}t}). \tag{2}$$

Here, q_0 is the maximum displacement of an atom from its equilibrium position, $\omega_{\text{ph}} = 194$ meV is the energy of the E_{2g} phonon mode, and $\hat{\mathbf{e}}$ is the normalized eigenvector for a particular phonon mode. From Figs. 1(c) and 1(d), it is clear that $\hat{\mathbf{e}}_{\text{iLO}} = [1, 0, -1, 0]/\sqrt{2}$ and $\hat{\mathbf{e}}_{\text{iTO}} = [0, 1, 0, -1]/\sqrt{2}$, in which the first (last) two elements are components of the A (B) atom.

Due to coherent phonon excitations, lattice dynamics causes temporal variations in the relative distance between atoms ($\mathbf{d}_i$). In this case, the corresponding time-dependent Hamiltonian within the tight-binding approximation can be written as [54–56]

$$\hat{\mathcal{H}}_{\mathbf{k}}(t) = -\gamma(t) \sum_{i\in nn} e^{i\mathbf{k}\cdot\mathbf{d}_i(t)} \hat{a}^\dagger_{\mathbf{k}} \hat{b}_{\mathbf{k}} + \text{H.c.} \tag{3}$$

Here, the hopping energy is modeled as an exponentially decaying function of the relative displacement between nearest-neighbor atoms as $\gamma(t) = \gamma_0\, e^{-[|\mathbf{d}_i(t)|-a]/\delta}$, in which δ is the width of the decay function chosen to be $0.184a_0$ [57].

The interaction among laser, electrons, and coherently excited phonon mode in graphene is modeled by solving the following equations of the single-particle density matrix. By updating the modified Hamiltonian as a result of the lattice dynamics, semiconductor Bloch equations in comoving frame $|n, \mathbf{k} + \mathbf{A}(t)\rangle$ are extended and equations of motion read as

$$\frac{d}{dt}\rho^{\mathbf{k}}_{vv} = i\mathbf{E}(t)\cdot\mathbf{d}_{vc}(\mathbf{k}_t, t)\rho^{\mathbf{k}}_{cv} + \text{c.c.}, \tag{4a}$$

$$\frac{d}{dt}\rho^{\mathbf{k}}_{cv} = \left[-i\varepsilon_{cv}(\mathbf{k}_t, t) - \frac{1}{T_2}\right]\rho^{\mathbf{k}}_{cv} + i\mathbf{E}(t)\cdot\mathbf{d}_{cv}(\mathbf{k}_t, t)\left[\rho^{\mathbf{k}}_{vv} - \rho^{\mathbf{k}}_{cc}\right]. \tag{4b}$$

Here, $\mathbf{E}(t)$ and $\mathbf{A}(t)$ are, respectively, the electric field and the vector potential corresponding to the laser field, which are related as $\mathbf{E}(t) = -d\mathbf{A}(t)/dt$, and $\mathbf{k}_t$ is the shorthand notation for $\mathbf{k} + \mathbf{A}(t)$. $\varepsilon_{cv}(\mathbf{k})$ and $\mathbf{d}_{cv}(\mathbf{k})$ are, respectively, the band-gap energy and dipole matrix elements between valence and conduction bands at $\mathbf{k}$. $\mathbf{d}_{cv}(\mathbf{k})$ is defined as $\mathbf{d}_{cv}(\mathbf{k}) = i\langle c, \mathbf{k}|\nabla_{\mathbf{k}}|v, \mathbf{k}\rangle$. Also, $\rho^{\mathbf{k}}_{cc}(t) = 1 - \rho^{\mathbf{k}}_{vv}(t)$ and $\rho^{\mathbf{k}}_{vc}(t) = \rho^{\mathbf{k}*}_{cv}(t)$.

A phenomenological term to take care of the interband decoherence is added with a constant dephasing time T_2. We calculate the matrix elements at each time step during temporal evolution of the coherently excited phonon mode, which results in the additional time dependence in the matrix elements. As long as the maximum displacement of the atoms are small and the time step is too small compared to the

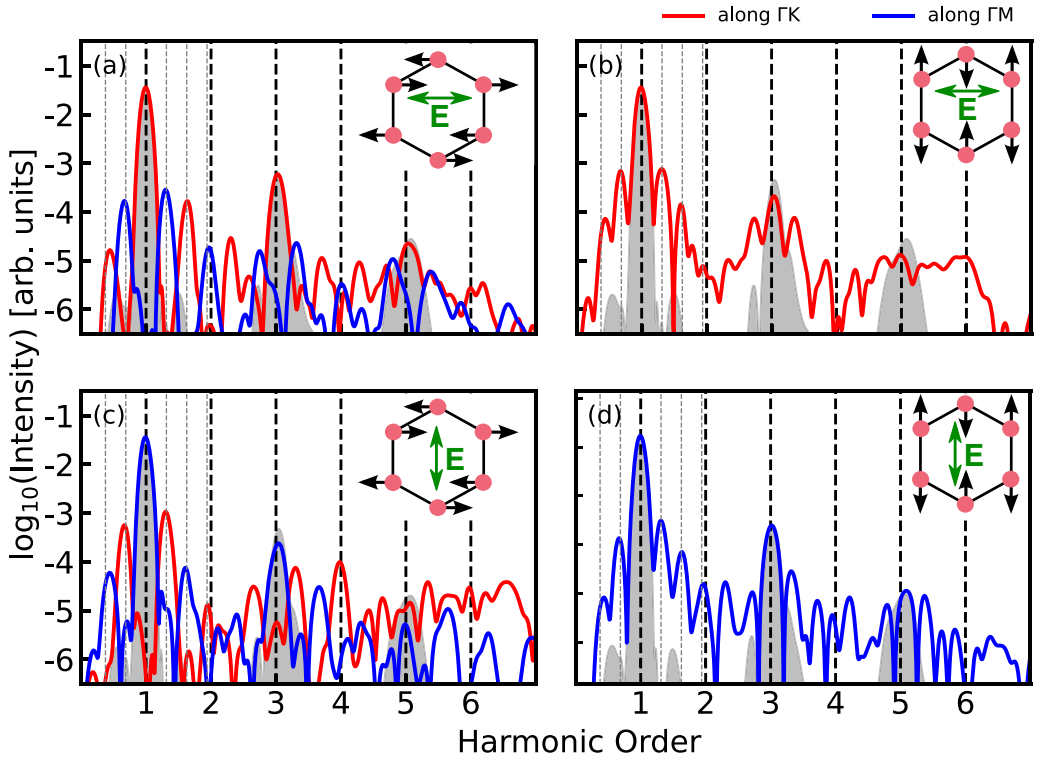

FIG. 2. High-harmonic spectra of monolayer graphene with and without coherent lattice dynamics. (a),(c) High-harmonic spectra corresponding to the coherent iLO E_{2g} phonon mode and the probe harmonic pulse is polarized along ΓK and ΓM directions, respectively. (b),(d) Same as (a) and (c) except iTO E_{2g} phonon mode is coherently excited. In all the cases, sidebands corresponding to the first harmonic are marked at frequencies $(\omega_0 \pm m\omega_{\rm ph})$, where ω_0 is the frequency of the harmonic generating probe pulse and $\omega_{\rm ph}$ is the phonon frequency. The harmonics with gray shaded area are the reference spectra and represent the spectra of graphene without phonon excitation. The unit cell of the graphene with the corresponding phonon eigenvector and polarization of the harmonic generating probe pulse are shown in the respective insets. Red (blue) color corresponds to the polarization of emitted radiation parallel (perpendicular) to the polarization of the harmonic generating probe pulse.

phonon time period, the matrix elements at consecutive time steps are smoothly updated.

We solve the coupled differential equations described in Eq. (4) using the fourth-order Runge-Kutta method with a time step of 0.01 fs. We sampled the Brillouin zone with a 251×251 grid. The current at any $\mathbf{k}$ point in the Brillouin zone is defined as

$$\mathbf{J}(\mathbf{k}, t) = \sum_{m,n\in\{c,v\}} \rho^{\mathbf{k}}_{mn}(t)\mathbf{p}_{nm}(\mathbf{k}_t, t). \tag{5}$$

Here, $\mathbf{p}_{nm}$ are the momentum matrix elements defined as $\mathbf{p}_{nm}(\mathbf{k}) = \langle n, \mathbf{k}|\nabla_{\mathbf{k}}\hat{\mathcal{H}}_{\mathbf{k}}|m, \mathbf{k}\rangle$. The total current, $\mathbf{J}$(t), can be calculated by integrating $\mathbf{J}(\mathbf{k}, t)$ over the entire Brillouin zone.

The high-harmonic spectrum is simulated as

$$\mathcal{I}(\omega) = \left|\mathcal{FT}\left(\frac{d}{dt}\mathbf{J}(t)\right)\right|^2. \tag{6}$$

Here, $\mathcal{FT}$ stands for the Fourier transform.

High-order harmonics are generated from monolayer graphene, with or without coherent lattice dynamics, using a linearly polarized pulse with a wavelength of 2.0 μm and peak intensity of 1×10^{11} W/cm^2. The pulse is 100 fs long and has a sin-squared envelope. The laser parameters used in this work are below the damage threshold of graphene [58]. Similar laser parameters have been used to investigate electron dynamics in graphene via intense laser pulse [59–61]. The value of the dephasing time $T_2 = 10$ fs is used throughout in this work [62]. The observations we made here are consistent for other values of T_2 in the range 5–30 fs. Both in-plane E_{2g} phonon modes are considered here. Results presented in this work correspond to a maximum $0.03a_0$ displacement of atoms from their equilibrium positions during coherent lattice dynamics. However, our findings remain valid for displacements ranging from $0.01a_0$ to $0.05a_0$ with respect to the equilibrium positions.

III. RESULTS AND DISCUSSION

High-harmonic spectra for monolayer graphene, with and without coherent lattice dynamics, are presented in Fig. 2. The spectrum corresponding to the graphene, without lattice dynamics, is shown by the gray shaded area as a reference. Owing to the inversion symmetry of the graphene, the reference spectrum in gray color exhibits only odd harmonics (consistent with earlier reports; e.g., Refs. [61–64]).

We assume that coherent phonon dynamics is excited prior to a high-harmonic probe. When one of the E_{2g} phonon modes in graphene is coherently excited, the harmonic spectra display sidebands along with the main odd harmonic peaks as reflected from Fig. 2. The energy difference between the adjacent sidebands matches the phonon energy ($\omega_{\rm ph}$). The sideband intensity is sensitive to the phonon amplitude but is

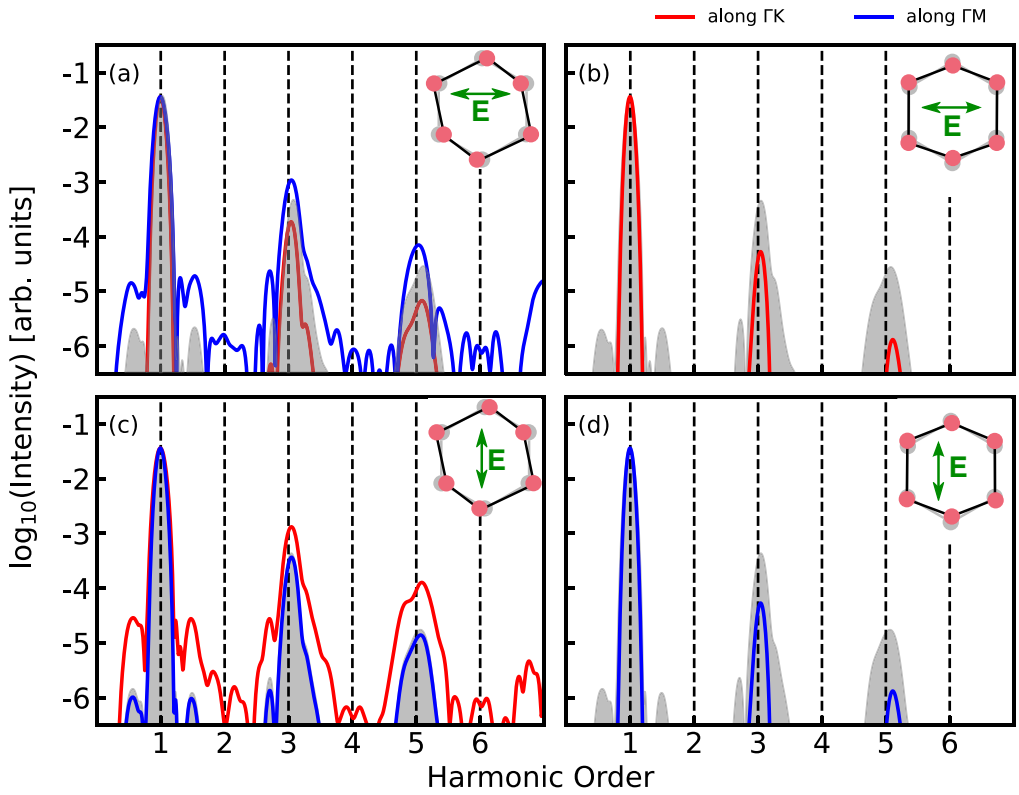

FIG. 3. High-harmonic spectra of monolayer deformed graphene. (a),(c) When the atoms in graphene are maximally displaced, from their equilibrium position, along iLO phonon mode. (b),(d) Similar to (a) and (b) but atoms are displaced along the iTO phonon mode. The harmonic spectrum of undeformed graphene is shown in the gray shaded area for reference. The unit cell of the deformed graphene lattice and the polarization of the harmonic generating probe pulse are shown in the respective insets. Red (blue) color corresponds to the polarization of emitted radiation parallel (perpendicular) to the polarization of the harmonic generating probe pulse.

clearly visible already for amplitudes above 0.01 of the lattice constant. Here we present the case of the amplitude equal to 0.03 of the lattice constant.

As E_{2g} phonon modes preserve the inversion center, only odd harmonics are generated. When the coherent iLO mode and the probe harmonic pulse (along $\Gamma - K$) are in the same direction, the even-order sidebands are polarized along $\Gamma - K$ (red color), whereas the odd-order sidebands are polarized perpendicular to $\Gamma - K$ (blue color), i.e., along the $\Gamma - M$ direction [see Fig. 2(a)]. When the polarization of the probe pulse changes from $\Gamma - K$ to $\Gamma - M$ direction, the polarization of the sidebands remains the same with respect to the laser polarization. In this case, the even-order sidebands are polarized along $\Gamma - M$ (blue color), whereas odd-order sidebands are polarized along $\Gamma - K$ (red color) [see Fig. 2(c)]. In both the cases, the main harmonic peaks are always polarized along the direction of the probe pulse.

The situation is simpler in the case of coherent iTO mode excitation. Both the main harmonic peaks and the sidebands are polarized along the direction of the probe pulse [see Figs. 2(b) and 2(d)]. Thus we see that the polarization of the sidebands yields information about the symmetries of the excited phonon modes.

We now investigate how the dynamical changes in symmetries differ from similar static variation in the high-harmonic spectra. Consider the static case with the maximum displacement of atoms, along a particular phonon mode direction, 3% of the lattice parameter from their equilibrium positions. Figure 3 compares high-harmonic spectra for the statically deformed and undeformed graphene (gray color). The probe polarization is along $\Gamma - K$ and $\Gamma - M$ directions in the top and bottom panels of Fig. 3, respectively.

When the graphene is deformed along the iLO phonon mode, odd harmonics are generated along parallel and perpendicular directions with respect to the laser polarization as shown in Figs. 3(a) and 3(c), respectively. However, only odd harmonics, parallel to the laser polarization, are generated when graphene is deformed in accordance with the iTO mode [see Figs. 3(b) and 3(d)].

The emergence of parallel and perpendicular components in the first case and the parallel component in the second case can be explained as follows: the monolayer graphene has σ_x and σ_y symmetry planes, in addition to the inversion center. When the polarization of the probe laser is along the high symmetry direction ($\Gamma - K$ or $\Gamma - M$), there is no perpendicular component of the current. However, if the polarization of the probe pulse is along any other than these high-symmetry directions, symmetry constraints allow the generation of odd harmonics perpendicular to the direction of the laser polarization. Recently, the same symmetry concept is employed in twisted bilayer graphene to correlate the twist angle with its high-harmonic spectrum [65]. It is straightforward to see that the distortion due to the iLO phonon mode breaks the symmetries of the reflection planes in monolayer graphene.

The absence of the reflection symmetry planes along X and Y directions guarantees the generation of harmonics in both $\Gamma - K$ and $\Gamma - M$ directions as shown in Figs. 3(a) and 3(c). On the other hand, the iTO phonon mode preserves both the symmetry planes and as a result harmonics along the laser polarization are only allowed [Figs. 3(b) and 3(d)].

In short, the presence or absence of the perpendicular current is a result of the transient breaking of the symmetry planes, which can be correlated to the results in Fig. 2. To understand the mechanism behind the sideband generations and associated polarization properties during a coherent lattice dynamics, we need to consider the changes in the symmetries dynamically during the probe pulse.

To understand the symmetry constraint on the polarization of sidebands, let us consider dynamical symmetries (DSs) of the system, accounting for the coherent lattice dynamics and the probe pulse. We apply the Floquet formalism to a periodically driven system, represented by the Hamiltonian described by Eq. (3), which satisfies $\hat{\mathcal{H}}_{\mathbf{k}}(t) = \hat{\mathcal{H}}_{\mathbf{k}}(t + \tau_{\rm ph})$, where $\tau_{\rm ph}$ is the time period corresponding to $\omega_{\rm ph}$. The Hamiltonian obeys the time-dependent Schrödinger equation and its solution is obtained in the basis of the Floquet states as $|\psi_n^{\rm F}(t)\rangle = e^{-i\epsilon_n^{\rm F} t}|\phi_n^{\rm F}(t)\rangle$. Here, $\epsilon_n^{\rm F}$ is the quasienergy corresponding to the nth Floquet state and $|\phi_n^{\rm F}(t)\rangle$ is the time-periodic part of the wave function, such that $|\phi_n^{\rm F}(t + \tau_{\rm ph})\rangle = |\phi_n^{\rm F}(t)\rangle$. The DSs in a Floquet system are the combined spatiotemporal symmetries, which provide different kinds of selection rules as discussed in Refs. [66,67].

In the presence of the probe pulse, the laser-graphene interaction within tight-binding approximation can be modeled with the Peierls substitution as $\hat{\mathcal{H}}_{\mathbf{k}}(t) \rightarrow \hat{\mathcal{H}}_{\mathbf{k}+\mathbf{A}(t)}(t)$. For the sake of simplicity, we employ a perturbative approach to understand the polarization of the sidebands as the strength of the sidebands is much weaker in comparison to the main harmonic peaks. Let us expand $\hat{\mathcal{H}}_{\mathbf{k}+\mathbf{A}(t)}(t)$ in terms of $i\mathbf{A}(t) \cdot \mathbf{d}_i(t)$ as

$$\hat{\mathcal{H}}_{\mathbf{k}+\mathbf{A}(t)}(t) \approx \hat{\mathcal{H}}_{\mathbf{k}}(t) + \mathbf{A}(t) \cdot \nabla_{\mathbf{k}} \hat{\mathcal{H}}_{\mathbf{k}}(t). \tag{7}$$

The second term in the above equation can be treated as a perturbation as $\hat{\mathcal{H}}'_{\mathbf{k}}(t) = \mathbf{A}(t) \cdot \hat{\mathbf{J}}(t)$ with $\hat{\mathbf{J}} = \nabla_{\mathbf{A}(t)} \hat{\mathcal{H}}_{\mathbf{k}+\mathbf{A}(t)}$ being the current operator in the Bloch basis. In Eq. (7), higher-order terms are neglected.

By following Ref. [67] and assuming the electron initially is in the Floquet state $|\phi_i^{\rm F}\rangle$, we can solve the time-dependent Schrödinger equation within first-order perturbation theory and the μth component of the current can be written as

$$J_\mu(t) = \langle \phi_i^{\rm F}(t) | \hat{J}_\mu(t) | \phi_i^{\rm F}(t) \rangle - \sum_{e \neq i} \int_{-\infty}^{t} i dt' e^{-i\omega_{ei}(t-t')} \chi_{\mu\nu}^{\rm F}(t, t') A_\nu(t') + \text{c.c.} \tag{8}$$

Here, $\chi_{\mu\nu}^{\rm F}(t, t') = \langle \phi_i^{\rm F}(t)|\hat{J}_\mu(t)|\phi_e^{\rm F}(t)\rangle \langle \phi_e^{\rm F}(t')|\hat{J}_\nu(t')|\phi_i^{\rm F}(t')\rangle$. From the above equation, it is apparent that the second term correlates to the generations of the sidebands via the Raman process.

The symmetry constraint for the mth-order sideband can be written as $\hat{X}^t \mathbf{E}_{s,m}(t)[\hat{X}^t \mathbf{E}(t)]^\dagger = \mathbf{E}_{s,m}\mathbf{E}^\dagger(t)$, provided spatial symmetries of $\hat{X}^t$ and probe pulse are the same [67]. Here, $\mathbf{E}_{s,m}(t)$ and $\mathbf{E}(t)$ are, respectively, the electric fields associated with mth-order sideband and the probe laser and $\hat{X}^t$ is the dynamical symmetry operation. The quantity $\mathbf{E}_{s,m}(t)\mathbf{E}(t)^\dagger$ is denoted by $\mathcal{R}_m(t)$ and known as the Raman tensor [67]. Thus the selection rules for the sidebands depend on the invariance of the Raman tensor under operation with the DSs of the Floquet system.

There are two DSs corresponding to the coherent iLO phonon mode as shown in Fig. 4. We define τ_n as the time translation of $\tau_{\rm ph}/n$, $\hat{C}_{n\mu}$ is the rotation of $2\pi/n$ with respect to the μ axis, $\hat{\sigma}_\mu$ is the reflection with respect to the μ axis, and $\hat{\mathcal{T}}$ is the time-reversal operator. The symmetry operations $\mathcal{D}_1 = \hat{\sigma}_x \cdot \tau_2$ [see Fig. 4(a)] and $\mathcal{D}_2 = \hat{\sigma}_x$ [see Fig. 4(b)] leave the system invariant.

The selection rules for the sidebands and its polarization directions are obtained from the DSs as shown in Fig. 4 and require a condition as $\hat{\mathcal{D}}\mathcal{R}_m(t) = \mathcal{R}_m(t)$. We assume that the temporal part of the mth-order sideband is $e^{i(\omega_0 \pm m\omega_{\rm ph})t + \phi_0}$ and of the probe laser pulse is $e^{i\omega_0 t}$. In such a situation, the Raman tensor is explicitly written as

$$\mathcal{R}_m(t) = e^{i(\pm m\omega_{\rm ph} t + \phi_0)} \begin{bmatrix} E_{s,m_x} E_x^* & E_{s,m_x} E_y^* \\ E_{s,m_y} E_x^* & E_{s,m_y} E_y^* \end{bmatrix}. \tag{9}$$

When the probe laser is polarized along the X axis, the invariance condition for the Raman tensor $\hat{\mathcal{D}}_1 \mathcal{R}_m(t) = \mathcal{R}_m(t)$ reduces to

$$e^{i(\pm m\omega_{\rm ph} t)} \begin{bmatrix} E_{s,m_x} \\ E_{s,m_y} \end{bmatrix} = e^{i[\pm m(\omega_{\rm ph} t + \pi)]} \begin{bmatrix} E_{s,m_x} \\ -E_{s,m_y} \end{bmatrix}. \tag{10}$$

The selection rule for the mth-order sideband is as follows: when m is odd (even), the polarization of the sideband will be along the Y(X) direction. Our observations in Fig. 2(a) are consistent with Eq. (10).

When the iLO phonon mode is excited and the probe pulse is along the $\Gamma - M$ direction, $\hat{\sigma}_y \cdot \tau_2$ and $\hat{C}_{2Z}$ are the DSs, which leave the Raman tensor invariant. It is straightforward to see that the selection rules for the mth-order sideband are deduced as follows: when m is odd (even), the polarization of the sidebands will be along the X(Y) direction. On the other hand, when the iTO phonon mode is excited and the probe pulse is along the $\Gamma - K$ ($\Gamma - M$) direction, $\hat{\sigma}_x$ ($\hat{\sigma}_y$) is the DS, which yields the Raman tensor invariant [see Fig. 4(b)]. This symmetry restricts the polarization of the sidebands to be along the direction of the probe pulse. Our results are consistent with the observation made in Fig. 2. With the increased intensity of the probe, higher-order harmonics and sidebands will appear.

To summarize, we have established that high-harmonic spectroscopy is responsive to the coherent lattice dynamics in solids. The high-harmonic spectrum is modulated by the frequency of the excited phonon mode within the solid. Both in-plane E_{2g} Raman-active phonon modes of the monolayer graphene lead to the generation of higher-order sidebands, along with the main harmonic peaks. In the case of iLO phonon mode excitation, the even- and odd-order sidebands are polarized parallel and perpendicular to the polarization of the probe harmonic pulse, respectively. In the case of the iTO phonon mode, all sidebands are polarized along the probe harmonic pulse's polarization. The polarizations of the sidebands are dictated by the dynamical symmetries of

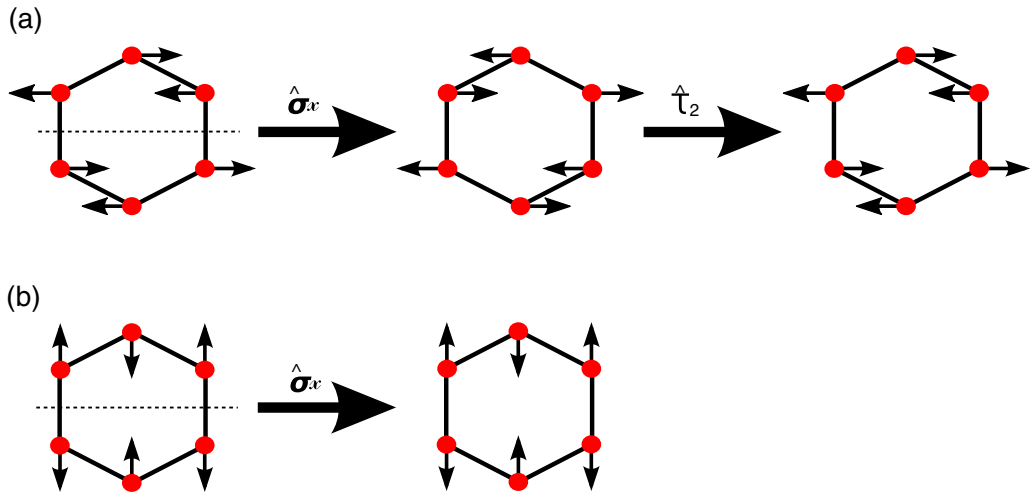

FIG. 4. Schematic representations of the dynamical symmetries of the Floquet Hamiltonian (a) $\hat{\mathcal{D}}_1 = \hat{\sigma}_x \cdot \hat{\tau}_2$ and (b) $\hat{\mathcal{D}}_2 = \hat{\sigma}_x$. The arrows show the displacements of the atom for a particular phonon mode.

the combined system, which includes the phonon modes and probe laser pulse. Therefore, the polarization properties are a sensitive probe of these dynamical symmetries. The presence of a high-harmonic signal perpendicular to the polarization of the probe pulse is a signature of lattice excitation-driven symmetry breaking of the reflection plane. The present work is paving a way for probing phonon-driven processes in solids and nonlinear phononics with subcycle temporal resolution.

ACKNOWLEDGMENTS

We acknowledge fruitful discussion with S. Pujari (IIT Bombay), D. Bansal (IIT Bombay), and K. Reimann (MBI Berlin). G.D. acknowledges support from Science and Engineering Research Board (SERB), India (Project No. MTR/2021/000138). D.K. acknowledges support from CRC 1375 "NOA–Nonlinear optics down to atomic scales," Project C4, funded by the Deutsche Forschungsgemeinschaft (DFG).

[1] M. Ferray, A. L'Huillier, X. F. Li, L. A. Lompre, G. Mainfray, and C. Manus, J. Phys. B: At., Mol., Opt. Phys. **21**, L31 (1988).
[2] S. Ghimire, A. D. DiChiara, E. Sistrunk, P. Agostini, L. F. DiMauro, and D. A. Reis, Nat. Phys. **7**, 138 (2011).
[3] G. Vampa, T. J. Hammond, N. Thiré, B. E. Schmidt, F. Légaré, C. R. McDonald, T. Brabec, D. D. Klug, and P. B. Corkum, Phys. Rev. Lett. **115**, 193603 (2015).
[4] T. T. Luu, M. Garg, S. Y. Kruchinin, A. Moulet, M. T. Hassan, and E. Goulielmakis, Nature (London) **521**, 498 (2015).
[5] A. A. Lanin, E. A. Stepanov, A. B. Fedotov, and A. M. Zheltikov, Optica **4**, 516 (2017).
[6] M. M. S., A. Pattanayak, M. Ivanov, and G. Dixit, Phys. Rev. A **100**, 043420 (2019).
[7] N. Tancogne-Dejean, O. D. Mücke, F. X. Kärtner, and A. Rubio, Phys. Rev. Lett. **118**, 087403 (2017).
[8] M. S. Mrudul, N. Tancogne-Dejean, A. Rubio, and G. Dixit, npj Comput. Mater. **6**, 10 (2020).
[9] A. Pattanayak, M. M. S., and G. Dixit, Phys. Rev. A **101**, 013404 (2020).
[10] M. Mrudul, Á. Jiménez-Galán, M. Ivanov, and G. Dixit, Optica **8**, 422 (2021).
[11] F. Langer, C. P. Schmid, S. Schlauderer, M. Gmitra, J. Fabian, P. Nagler, C. Schüller, T. Korn, P. Hawkins, J. Steiner *et al.*, Nature (London) **557**, 76 (2018).
[12] M. S. Mrudul and G. Dixit, J. Phys. B: At., Mol., Opt. Phys. **54**, 224001 (2021).
[13] O. Schubert, M. Hohenleutner, F. Langer, B. Urbanek, C. Lange, U. Huttner, D. Golde, T. Meier, M. Kira, S. W. Koch, and R. Huber, Nat. Photon. **8**, 119 (2014).
[14] D. Bauer and K. K. Hansen, Phys. Rev. Lett. **120**, 177401 (2018).
[15] N. Tancogne-Dejean, M. A. Sentef, and A. Rubio, Phys. Rev. Lett. **121**, 097402 (2018); Y. Murakami, M. Eckstein, and P. Werner, *ibid.* **121**, 057405 (2018).
[16] Y. Bai, F. Fei, S. Wang, N. Li, X. Li, F. Song, R. Li, Z. Xu, and P. Liu, Nat. Phys. **17**, 311 (2021).
[17] S. Imai, A. Ono, and S. Ishihara, Phys. Rev. Lett. **124**, 157404 (2020).
[18] M. Borsch, C. P. Schmid, L. Weigl, S. Schlauderer, N. Hofmann, C. Lange, J. T. Steiner, S. W. Koch, R. Huber, and M. Kira, Science **370**, 1204 (2020).
[19] D. Baykusheva, A. Chacón, J. Lu, T. P. Bailey, J. A. Sobota, H. Soifer, P. S. Kirchmann, C. Rotundu, C. Uher, T. F. Heinz *et al.*, Nano Lett. **21**, 8970 (2021).
[20] A. Bharti, M. M. S., and G. Dixit, Phys. Rev. B **105**, 155140 (2022).
[21] A. Pattanayak, S. Pujari, and G. Dixit, Sci. Rep. **12**, 6722 (2022).
[22] A. Chacón, D. Kim, W. Zhu, S. P. Kelly, A. Dauphin, E. Pisanty, A. S. Maxwell, A. Picón, M. F. Ciappina, D. E. Kim *et al.*, Phys. Rev. B **102**, 134115 (2020).
[23] C. Shao, H. Lu, X. Zhang, C. Yu, T. Tohyama, and R. Lu, Phys. Rev. Lett. **128**, 047401 (2022).
[24] H. Lakhotia, H. Y. Kim, M. Zhan, S. Hu, S. Meng, and E. Goulielmakis, Nature (London) **583**, 55 (2020).
[25] R. Mankowsky, M. Först, and A. Cavalleri, Rep. Prog. Phys. **79**, 064503 (2016).

[26] R. Hollinger, V. Shumakova, A. Pugžlys, A. Baltuška, S. Khujanov, C. Spielmann, and D. Kartashov, in EPJ Web of Conferences **205**, 02025 (2019).

[27] S. Patchkovskii, Phys. Rev. Lett. **102**, 253602 (2009).

[28] N. L. Wagner, A. Wüest, I. P. Christov, T. Popmintchev, X. Zhou, M. M. Murnane, and H. C. Kapteyn, Proc. Natl. Acad. Sci. U.S.A. **103**, 13279 (2006).

[29] A.-T. Le, T. Morishita, R. R. Lucchese, and C. D. Lin, Phys. Rev. Lett. **109**, 203004 (2012).

[30] S. Baker, J. S. Robinson, C. Haworth, H. Teng, R. Smith, C. C. Chirila, M. Lein, J. Tisch, and J. P. Marangos, Science **312**, 424 (2006).

[31] M. Lein, Phys. Rev. Lett. **94**, 053004 (2005).

[32] H. J. Wörner, J. B. Bertrand, B. Fabre, J. Higuet, H. Ruf, A. Dubrouil, S. Patchkovskii, M. Spanner, Y. Mairesse, V. Blanchet *et al.*, Science **334**, 208 (2011).

[33] J. Niedziela, D. Bansal, A. May, J. Ding, T.L.-Atkins, G. Ehlers, D. Abernathy, A. Said, and O. Delaire, Nat. Phys. **15**, 73 (2019).

[34] M. Dove, *Introduction to Lattice Dynamics* (Cambridge University Press, Cambridge, UK, 1993).

[35] H. Katsuki, J. Delagnes, K. Hosaka, K. Ishioka, H. Chiba, E. Zijlstra, M. Garcia, H. Takahashi, K. Watanabe, M. Kitajima *et al.*, Nat. Commun. **4**, 2801 (2013).

[36] D. Bansal, J. L. Niedziela, S. Calder, T. Lanigan-Atkins, R. Rawl, A. H. Said, D. L. Abernathy, A. I. Kolesnikov, H. Zhou, and O. Delaire, Nat. Phys. **16**, 669 (2020).

[37] M. Hase, P. Fons, K. Mitrofanov, A. V. Kolobov, and J. Tominaga, Nat. Commun. **6**, 8367 (2015).

[38] D. Bansal, J. Niedziela, R. Sinclair, V. Garlea, D. Abernathy, S. Chi, Y. Ren, H. Zhou, and O. Delaire, Nat. Commun. **9**, 15 (2018).

[39] B. Fultz, Prog. Mater. Sci. **55**, 247 (2010).

[40] A. Gambetta, C. Manzoni, E. Menna, M. Meneghetti, G. Cerullo, G. Lanzani, S. Tretiak, A. Piryatinski, A. Saxena, R. Martin *et al.*, Nat. Phys. **2**, 515 (2006).

[41] L. Dhar, J. A. Rogers, and K. A. Nelson, Chem. Rev. **94**, 157 (1994).

[42] T. Debnath, D. Sarker, H. Huang, Z.-K. Han, A. Dey, L. Polavarapu, S. V. Levchenko, and J. Feldmann, Nat. Commun. **12**, 2629 (2021).

[43] D. Graf, F. Molitor, K. Ensslin, C. Stampfer, A. Jungen, C. Hierold, and L. Wirtz, Nano Lett. **7**, 238 (2007).

[44] A. Virga, C. Ferrante, G. Batignani, D. De Fazio, A. Nunn, A. Ferrari, G. Cerullo, and T. Scopigno, Nat. Commun. **10**, 3658 (2019).

[45] J. Koivistoinen, P. Myllyperkio, and M. Pettersson, J. Phys. Chem. Lett. **8**, 4108 (2017).

[46] N. Rana, A. P. Roy, D. Bansal, and G. Dixit, npj Comput. Mater. **7**, 7 (2021).

[47] S. B. Brown, A. Gleason, E. Galtier, A. Higginbotham, B. Arnold, A. Fry, E. Granados, A. Hashim, C. G. Schroer, A. Schropp *et al.*, Sci. Adv. **5**, eaau8044 (2019).

[48] D. J. Flannigan, Physics **11**, 53 (2018).

[49] I. Gierz, M. Mitrano, H. Bromberger, C. Cacho, R. Chapman, E. Springate, S. Link, U. Starke, B. Sachs, M. Eckstein *et al.*, Phys. Rev. Lett. **114**, 125503 (2015).

[50] E. Pomarico, M. Mitrano, H. Bromberger, M. A. Sentef, A. Al-Temimy, C. Coletti, A. Stöhr, S. Link, U. Starke, C. Cacho, R. Chapman, E. Springate, A. Cavalleri, and I. Gierz, Phys. Rev. B **95**, 024304 (2017).

[51] A. Moulet, J. B. Bertrand, T. Klostermann, A. Guggenmos, N. Karpowicz, and E. Goulielmakis, Science **357**, 1134 (2017).

[52] R. Géneaux, C. J. Kaplan, L. Yue, A. D. Ross, J. E. Bækhøj, P. M. Kraus, H.-T. Chang, A. Guggenmos, M.-Y. Huang, M. Zürch *et al.*, Phys. Rev. Lett. **124**, 207401 (2020).

[53] J.-H. Kim, A. Nugraha, L. Booshehri, E. Hároz, K. Sato, G. Sanders, K.-J. Yee, Y.-S. Lim, C. Stanton, R. Saito *et al.*, Chem. Phys. **413**, 55 (2013).

[54] V. Mohanty and E. J. Heller, Proc. Natl. Acad. Sci. USA **116**, 18316 (2019).

[55] M. Rodriguez-Vega, M. Vogl, and G. A. Fiete, Phys. Rev. B **104**, 245135 (2021).

[56] J. Wang and S. Fischer, Phys. Rev. B **89**, 245421 (2014).

[57] P. Moon and M. Koshino, Phys. Rev. B **87**, 205404 (2013).

[58] M. Currie, J. D. Caldwell, F. J. Bezares, J. Robinson, T. Anderson, H. Chun, and M. Tadjer, Appl. Phys. Lett. **99**, 211909 (2011).

[59] C. Heide, T. Higuchi, H. B. Weber, and P. Hommelhoff, Phys. Rev. Lett. **121**, 207401 (2018).

[60] T. Higuchi, C. Heide, K. Ullmann, H. B. Weber, and P. Hommelhoff, Nature (London) **550**, 224 (2017).

[61] N. Yoshikawa, T. Tamaya, and K. Tanaka, Science **356**, 736 (2017).

[62] M. M. S. and G. Dixit, Phys. Rev. B **103**, 094308 (2021).

[63] Y. Murakami and M. Schüler, Phys. Rev. B **106**, 035204 (2022).

[64] I. Al-Naib, J. E. Sipe, and M. M. Dignam, Phys. Rev. B **90**, 245423 (2014).

[65] M. Du, C. Liu, Z. Zeng, and R. Li, Phys. Rev. A **104**, 033113 (2021).

[66] O. Neufeld, D. Podolsky, and O. Cohen, Nat. Commun. **10**, 405 (2019).

[67] K. Nagai, K. Uchida, N. Yoshikawa, T. Endo, Y. Miyata, and K. Tanaka, Commun. Phys. **3**, 137 (2020).